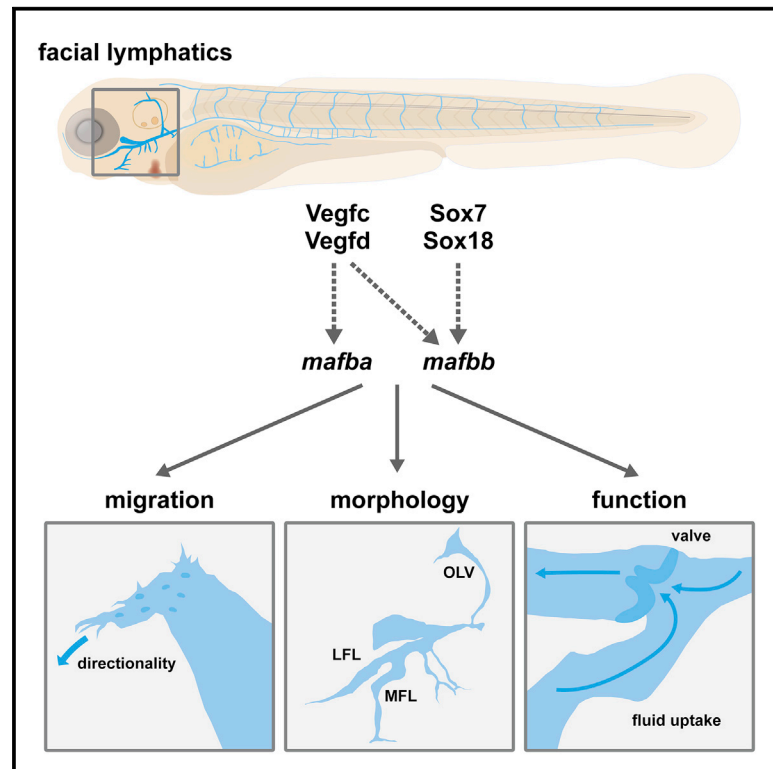


mafba and *mafbb* differentially regulate lymphatic endothelial cell migration in topographically distinct manners

Graphical abstract



Authors

Hannah Arnold, Virginia Panara, Melina Hußmann, ..., Benjamin M. Hogan, Stefan Schulte-Merker, Katarzyna Koltowska

Correspondence

kaska.koltowska@igp.uu.se

In brief

Arnold et al. investigate the role of transcription factors *Mafba* and *Mafbb* during lymphatic development. Using zebrafish mutants and live imaging in conjunction with molecular analysis, they identify topographically distinct requirements of these transcription factors. In the face, *mafba* and *mafbb* steer the direction of lymphatic endothelial cell migration.

Highlights

- *mafba* and *mafbb* are required for facial lymphatic development and function
- *mafbb* is dispensable for lymphatic development in the trunk
- *mafba* and *mafbb* regulate directionality of lymphatic endothelial cell migration
- Differential signaling regulates *mafba* and *mafbb* facial lymphangiogenesis



Report

mafba and *mafbb* differentially regulate lymphatic endothelial cell migration in topographically distinct manners

Hannah Arnold,¹ Virginia Panara,¹ Melina Hußmann,² Beata Filipek-Gorniok,³ Renae Skoczylas,¹ Petter Ranefall,⁴ Marleen Gloger,¹ Amin Allalou,⁴ Benjamin M. Hogan,^{5,6} Stefan Schulte-Merker,² and Katarzyna Koltowska^{1,7,*}

¹Immunology Genetics and Pathology, Uppsala University, Uppsala, Sweden

²Institute of Cardiovascular Organogenesis and Regeneration, WWU Münster, Medical Faculty, Münster, Germany

³Department of Organismal Biology, Uppsala University, Uppsala, Sweden

⁴Department of Information Technology, Division of Visual Information and Interaction, and SciLifeLab BiImage Informatics Facility, Uppsala University, Uppsala, Sweden

⁵Department of Anatomy and Physiology and Sir Peter MacCallum Department of Oncology, University of Melbourne, Melbourne, VIC 3000, Australia

⁶Organogenesis and Cancer Program, Peter MacCallum Cancer Centre, Melbourne, VIC 3000, Australia

⁷Lead contact

*Correspondence: kaska.koltowska@igp.uu.se

<https://doi.org/10.1016/j.celrep.2022.110982>

SUMMARY

Lymphangiogenesis, formation of lymphatic vessels from pre-existing vessels, is a dynamic process that requires cell migration. Regardless of location, migrating lymphatic endothelial cell (LEC) progenitors probe their surroundings to form the lymphatic network. Lymphatic-development regulation requires the transcription factor MAFB in different species. Zebrafish *Mafba*, expressed in LEC progenitors, is essential for their migration in the trunk. However, the transcriptional mechanism that orchestrates LEC migration in different lymphatic endothelial beds remains elusive. Here, we uncover topographically different requirements of the two paralogs, *Mafba* and *Mafbb*, for LEC migration. Both *mafba* and *mafbb* are necessary for facial lymphatic development, but *mafbb* is dispensable for trunk lymphatic development. On the molecular level, we demonstrate a regulatory network where *Vegfc-Vegfd-SoxF-Mafba-Mafbb* is essential in facial lymphangiogenesis. We identify that *mafba* and *mafbb* tune the directionality of LEC migration and vessel morphogenesis that is ultimately necessary for lymphatic function.

INTRODUCTION

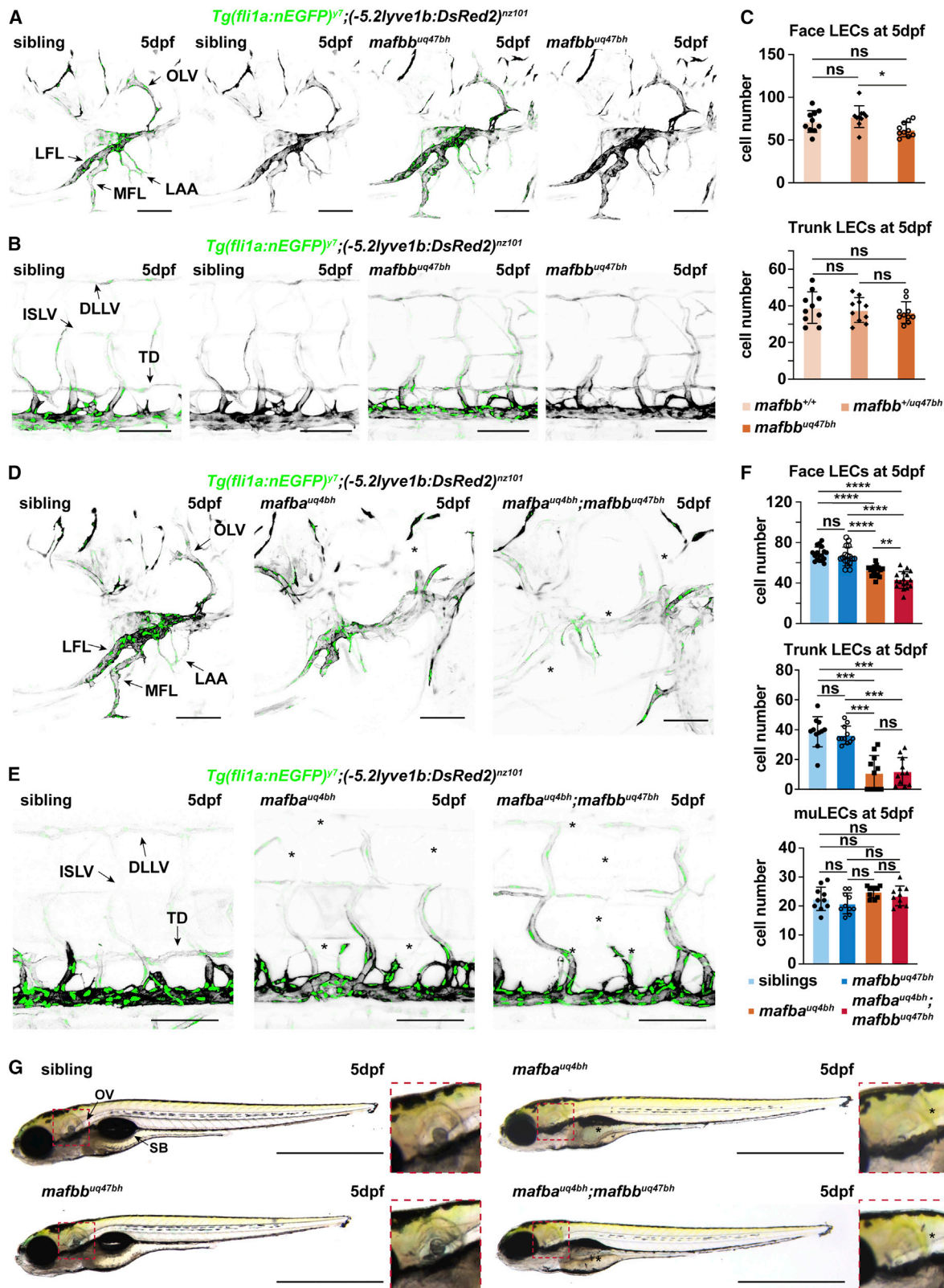
Lymphatic vascular networks are found in the majority of tissues and organs, and their functions include immune surveillance, body fluid homeostasis, and fat absorption (Koltowska et al., 2013). The diverse functionality of lymphatic vessels is achieved by distinct morphological features across the network. Despite these differences, the current dogma states that common molecular mechanisms drive lymphatic development.

Both in zebrafish and mouse, lymphatic vessels originate from different sources. Lineage-tracing studies in mice have shown that lymphatic endothelial cells (LECs) originate from veins (Karkainen et al., 2004; Wigle and Oliver, 1999), but also in heart, skin, and mesentery, they can be derived from a non-venous origin (Klotz et al., 2015; Martinez-Corral et al., 2015; Pichol-Thievend et al., 2018; Stanczuk et al., 2015). Zebrafish lymphatic development is studied primarily in two beds, face and trunk, which are morphologically distinct. Developing trunk lymphatics originate solely from the posterior cardinal vein (PCV) and form the trunk lymphatic network, consisting of the thoracic duct (TD), the dorsal longitudinal lymphatic vessel (DLLV), and the intersegmental

lymphatic vessels (ISLVs) (Küchler et al., 2006; Yaniv et al., 2006). The facial lymphatics arise from venous origins, the common cardinal vein (CCV) and the primary head sinus (PHS), and from a non-venous origin, the ventral aorta lymphangioblast (VA-L) (Eng et al., 2019; Okuda et al., 2012). The facial LEC progenitors come together to form the lateral facial lymphatic (LFL), the medial facial lymphatic (MFL), the lymphatic branchial arches (LAAs), and the otolithic lymphatic vessel (OLV) (Okuda et al., 2012). Noticeably, regardless of the origin, lymphatic-vessel identity is marked by the transcription factor *Prox1* (Koltowska et al., 2015a; Martinez-Corral et al., 2015; Pichol-Thievend et al., 2018; Shin et al., 2016; Wigle and Oliver, 1999). Moreover, the *Vegfc-Vegfr3* signaling cascade is required for LEC sprouting, proliferation, and migration (Karaman et al., 2018; Koltowska et al., 2013). Thus, common molecular mechanisms regulate main lymphangiogenesis in different species.

Recent work in zebrafish has uncovered signaling nuances in the regulation of face and trunk lymphatic development. Experiments disrupting *Vegfc* and *Vegfd* signaling have revealed their differential requirements during lymphangiogenesis (Astin et al., 2014; Bower et al., 2017a, 2017b; Shin et al., 2016). Moreover,





(legend on next page)

facial lymphangiogenesis is dependent on both *Vegfc* and *Vegfd* signaling via their receptors *Kdr* and *Flt4* (orthologs of *Vegfr2* and *Vegfr3*) (Bower et al., 2017a, 2017b; Vogrin et al., 2019). In contrast, trunk lymphangiogenesis is regulated by *Vegfc* signaling through *Flt4*. Thus, a ligand's ability to compensate for the other is location dependent. It remains unclear if these topographical requirements for different ligands and receptors are precursors to unique downstream transcriptional outputs.

Work from Koltowska et al. (2015b) uncovered that the transcription factor *Mafba* is part of the *Vegfc*-*SoxF* pathway and is essential for trunk LEC migration. Intriguingly, the facial lymphatic phenotype in *mafba* mutants is mild, with only a slight reduction in the LFL, MLF, and OLV, suggesting that other transcription factors are required for the formation of this lymphatic bed. Similarly, in mouse, *Mafb* regulates morphogenesis of a subset of lymphatic beds, including the skin and diaphragm (Dieterich et al., 2020; Rondon-Galeano et al., 2020), further supporting that a lymphatic-bed-specific transcriptional code may exist. As a consequence of the Teleost whole-genome duplication, *Mafb* has two paralogs in zebrafish, *mafba* and *mafbb*. *mafbb* remains expressed in *mafba* mutants and therefore serves as a promising candidate to explore in lymphatic-bed-specific development.

Here, we exploit the transcription factors *Mafba* and *Mafbb* as a model to uncover molecular mechanisms orchestrating lymphatic development in a topographically dependent manner. We uncovered a unique transcriptional requirement for the development of different lymphatic beds, with *mafba* and *mafbb* together directing facial lymphatic development. We show that, mechanistically, *Mafba* and *Mafbb* are required for directional migration of LECs in the facial lymphatics but not for their motility. The differential lymphangiogenic requirement of *mafba* and *mafbb* in the face and trunk creates possibilities for understanding how diversity is generated between lymphatic beds.

RESULTS AND DISCUSSION

mafbb has a compensatory role in lymphatic development in the facial lymphatic bed

We have previously shown that *mafbb* is expressed in *mafba* mutant endothelium (Koltowska et al., 2015b). To assess the role of *mafbb* in lymphatic development, we generated *mafbb* mutants using CRISPR-Cas9 technology. We introduced a 10

base pair (bp) deletion in the critical basic region leucine zipper (BRLZ) (Figure S1A), creating a premature stop codon resulting in a predicted loss-of-function allele. Phenotypic analysis of *Tg(-5.2lyve1b:DsRed2)* and *Tg(fli1a:nEGFP)* transgenic zebrafish lines at 5 days post-fertilization (dpf) revealed morphologically intact facial lymphatics in *mafbb* mutants with a small decrease in cell number compared with *mafbb* heterozygotes (Figures 1A and 1C). Trunk lymphatic development and cell number was unperturbed in *mafbb* mutants (Figures 1B and 1C). *mafbb* mutants have normal gross morphology (Figure 1G), growing into viable adults (Figure S1E). To test for maternal contribution, we crossed *mafbb* mutant females with *mafbb* heterozygous males, observing no additional phenotypes (data not shown). Therefore, *mafbb* loss is likely compensated by its paralog, *mafba*.

To investigate the facial LEC phenotype and address compensation, we generated *mafba;mafbb* double mutants and found more severe facial lymphatic phenotypes. *mafba;mafbb* mutants have a 35.9% LEC reduction compared with siblings (Figures 1F and S1B) and disrupted morphology (Figure 1D) compared with *mafba* mutants with a 25% reduction in face LECs (Figures 1F and S1B) with relatively unaffected morphology (Figure 1D). In addition, *mafba;mafbb* mutants have weaker *Tg(-5.2lyve1b:DsRed2)* expression than siblings or single mutants (Figure S1F). *mafba;mafbb* double-mutant trunk lymphatics show similar LEC numbers compared with *mafba* mutants at 5 dpf (Figures 1E, 1F, and S1C). This suggests that there are topographical differences in *mafba* and *mafbb* requirements across lymphatic vessels.

To investigate differences in other LEC derivatives, we have focused on mural LECs (muLECs), also known as fluorescent granular perihelical cells or brain LECs (Bower et al., 2017a; Galanter et al., 2017; van Lessen et al., 2017). This revealed that muLEC development was unaffected in *mafba*, *mafbb*, or double mutants (Figures 1F and S1G), indicating that muLEC migration is independent of *Mafba* and *Mafbb* regulation. Survival severity is comparable between *mafba;mafbb* double mutants and *mafba* mutants, and both genotypes show otolithic vesicle (OV) enlargement and absent swim bladders (Figures 1G and S1E). Quantitative real-time PCR did not reveal a striking upregulation of *mafba* in *mafbb* mutants, or vice versa (Figure S1D). Thus, we speculate that these two genes play specific roles during facial lymphatic-vessel development rather than follow the mechanisms of genetic compensation. Our findings reveal different

Figure 1. *mafba* and *mafbb* are required for facial lymphatic development

(A and B) Confocal images of (A) face and (B) trunk lymphatics labeled with *Tg(fli1a:nEGFP)* (endothelial nuclei, green) and *Tg(-5.2lyve1b:DsRed2)* (VECs and LECs, grey) in sibling and *mafbb* mutants at 5 dpf. LFL, lateral facial lymphatic; MFL, medial facial lymphatic; LAA, branchial lymphatic arches; OLV, otolithic lymphatic vessel; DLLV, dorsal longitudinal lymphatic vessel; ISLV, intersegmental lymphatic vessel; TD, thoracic duct. Scale bars, 100 μ m.

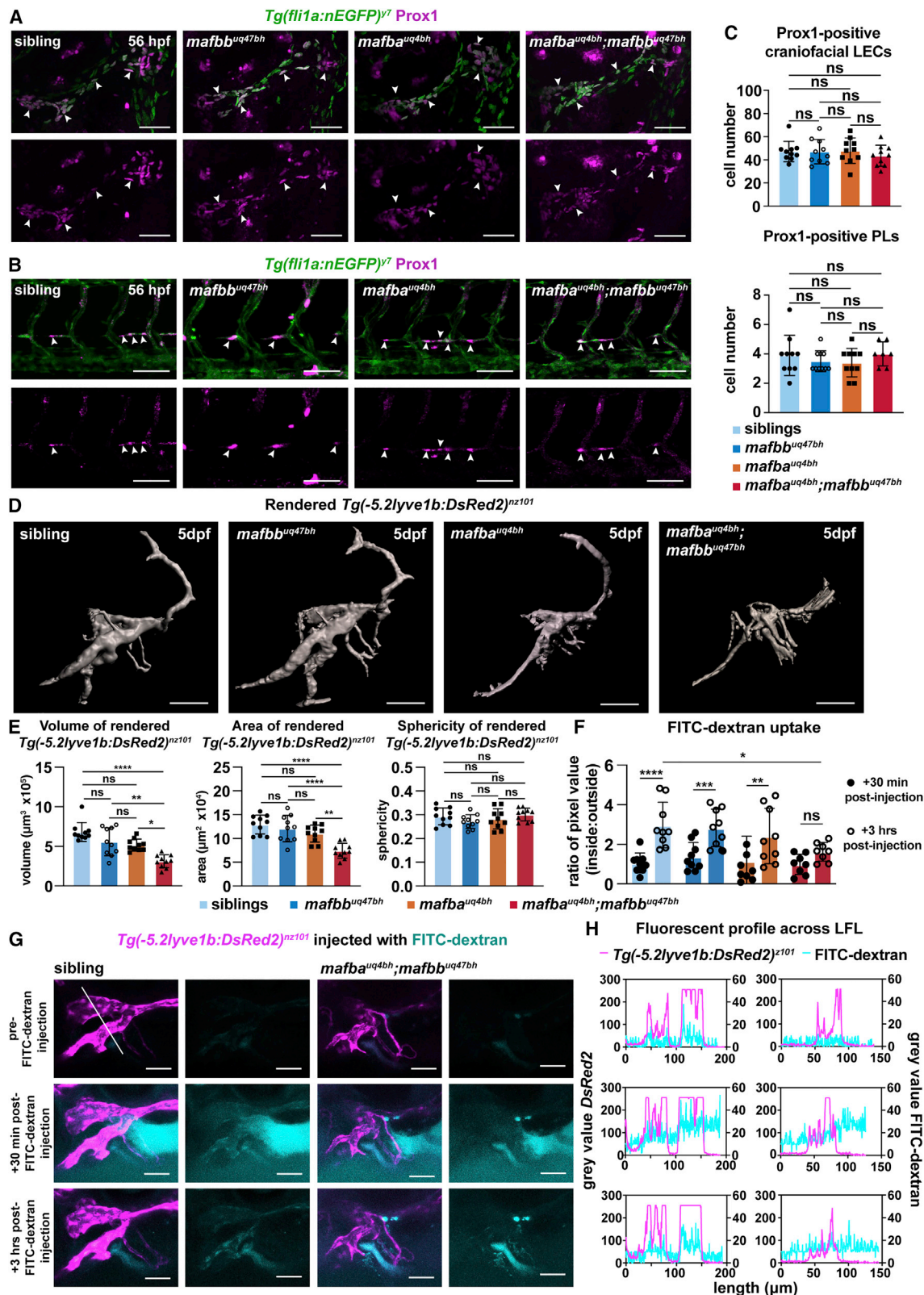
(C) Quantification of LECs in the face and trunk based on (A) in wild-type (*mafbb*^{+/+}), *mafbb* heterozygous (*mafbb*^{+/^{uq47bh}}), and *mafbb* homozygous mutants (*mafbb*^{uq47bh/uq47bh}) at 5 dpf. Embryos per genotypes; n = 10. One-way ANOVA: *p = 0.0174 for *mafbb*^{+/^{uq47bh}} versus *mafbb*^{uq47bh/uq47bh} in face LECs, ns p \geq 0.177 for other comparisons.

(D and E) Confocal images of (D) facial and (E) trunk lymphatics at 5 dpf for siblings and *mafba* and *mafba;mafbb* mutants. Transgenic markers described in (A). *: absent lymphatics. Scale bars, 100 μ m.

(F) LEC quantification at 5 dpf; embryos per genotype; n = 17 (face), n = 11 (trunk), n = 10 (muLECs). One-way ANOVA: p values for facial LECs: ns p = 0.7733 for siblings versus *mafbb* mutants; ****p < 0.0001 for siblings versus *mafba* or *mafba;mafbb* mutants and for *mafbb* versus *mafba* or *mafba;mafbb* mutants; **p < 0.0047 for *mafba* versus *mafba;mafbb* mutants. p values for trunk LECs: ***p \leq 0.0004 for siblings versus *mafba* or *mafba;mafbb* and *mafba* versus *mafbb* mutants; **p \leq 0.0029 for *mafbb* versus *mafba;mafbb* mutants. Other comparisons: ns p \geq 0.9999. Kruskal-Wallis test for muLECs: ns p = 0.070.

(G) Gross morphology of embryos at 5 dpf. *: absent structures; OV, otolithic vesicle; SB, swim bladder. Scale bars, 1 mm. ns, non-significant; stars are significant; error bars are mean \pm SD.

See also Figure S1.



(legend on next page)

regulatory requirements of lymphatic-vessel formation: *mafba* is needed for trunk lymphatic development, while both *mafbb* and *mafba* regulate facial lymphatic development.

LEC progenitors are specified independently of *mafba* and *mafbb*

LEC progenitors are still specified in the trunk of *mafba* mutants and make their way to the horizontal myoseptum (Koltowska et al., 2015b). We asked if the phenotypic severity in *mafba*;*-mafbb* double mutants originates from LEC-progenitor specification. Using *Tg(fli1a:nEGFP)* and immunostaining for Prox1 at 56 h post-fertilization (hpf) (Figures 2A and 2B), we found specified LECs in both beds for all mutant backgrounds (Figures 2A and 2B). Quantification of double-positive cells in the trunk and face revealed no difference in LEC numbers across all genotypes (Figure 2C), even when normalized to the total number of *Tg(fli1a:nEGFP)*-positive cells within the CCV and facial lymphatic sprout (FLS) (Figure S2A). Defects in proliferation in *mafba*;*mafbb* double mutants were ruled out by EdU staining (Figure S2B). Thus, *mafba* and *mafbb* are required for lymphatic development after LEC-progenitor specification.

Facial lymphatic-vessel morphology is disrupted in *mafba*;*mafbb* mutants

To dissect how regulation by *mafba* and *mafbb* is translated into tissue organization, we measured different morphological features of the developing facial lymphatic vessels. Surface rendering of *Tg(-5.2lyve1b:DsRed2)* revealed that the facial lymphatic network was disrupted, with thinner and mis-shaped vessels in *mafba*;*mafbb* mutants (Figure 2D). The facial lymphatic vessels are shorter and globular with volume and area reduced by half compared with siblings; however, sphericity was unaltered across the mutant backgrounds (Figure 2E; Video S1). Together, these findings reveal that *mafba* and *mafbb* are required for craniofacial lymphatic-vessel morphogenesis and proper vessel organization.

Lymphatic function is disrupted in *mafba*;*mafbb* mutants

We speculated that the dysmorphic vessels in *mafba*;*mafbb* mutants would impact lymphatic function. To test functionality, we

injected fluorescein isothiocyanate (FITC)-dextran into the tissue ventral to the LFL and in between the LAA at 5 dpf. We found no difference in FITC-dextran uptake after 30 min between the different genotypes. However, after 3 h, the uptake in the double mutants was significantly reduced compared with the other genotypes (Figures 2F–2H and S2C). Moreover, while fluid uptake in siblings, *mafba* mutants, and *mafbb* mutants significantly increased from 30 min to 3 h, there was no change in uptake over time in *mafba*;*mafbb* mutants (Figure 2F). The uptake defects were independent of the reduction in vessel size in *mafba*;*mafbb* mutants (Figure S2D). These results were confirmed by injection of Qtracker 655 Vascular Labels (hereafter referred to as Qtracker) at 5 dpf (Figures S2E and S2F). These data suggest that the reduced volume and altered morphology of *mafba*;*mafbb* mutants impacts their ability to remove fluid from the surroundings at the appropriate rate.

mafba and *mafbb* regulate lymphatic-vessel maturation

Defective vessel morphology in *mafba*;*mafbb* mutants was further validated with the transgenic line *TgBAC(prox1a:KalTA4-4xUAS-ADV.E1b:TagRFP)* (hereafter referred to as *Tg(prox1a:RFP)*, reporting *prox1a* expression in the developing lymphatic vasculature. *prox1a* is expressed in all backgrounds at 5 dpf, and the facial lymphatic phenotypes recapitulated those observed in *Tg(-5.2lyve1b:DsRed2)* transgenic fish (Figure 3A). A newly discovered morphological feature of facial lymphatics is a valve (Shin et al., 2019). *Tg(prox1a:RFP)* is expressed in the developing valve at 5 dpf, which appeared to be mis-patterned with 55.1% length reduction in *mafba*;*mafbb* mutants compared with siblings (Figures 3A and 3B). To analyze valve morphology, we generated average phenotype images by computationally overlaying single images from siblings and *mafbb*, *mafba*, and *mafba*;*mafbb* mutants (Figures 3C, 3D, S2G, and S2H). We observed a graduated phenotype from siblings and *mafbb* mutants (narrow valve) to *mafba*;*mafbb* mutants (unclear valve), in which *mafba* mutants (broad valve) are a hybrid of the two phenotypes, with increasing phenotypic variability across genotypes (Figures 3C, 3D, and S2G; Video S2). To test valve functionality in the different genetic backgrounds, we injected Qtracker into the facial lymphatic vessels (FLVs) of anaesthetized embryos and imaged 5 min post-injection (Figure 3E). We observed a 70.6%

Figure 2. *mafba* and *mafbb* regulate lymphatic-vessel morphology and function but not specification

(A and B) Prox1-positive LECs (magenta) (arrows) co-labeled with *Tg(fli1a:nEGFP)* (green) at 56 hpf in (A) face and (B) trunk in siblings and *mafbb*, *mafba*, and double mutants. Scale bars, 50 μ m.

(C) LEC progenitors quantification of Prox1 and *Tg(fli1a:nEGFP)* double-positive cells. Embryos per genotype; n = 10; Kruskal-Wallis test: ns p \geq 0.5331.

(D) Surface rendering of *Tg(-5.2lyve1b:DsRed2)* for siblings and *mafbb*, *mafba*, and double mutants from confocal z stack images at 5 dpf. Scale bars, 100 μ m.

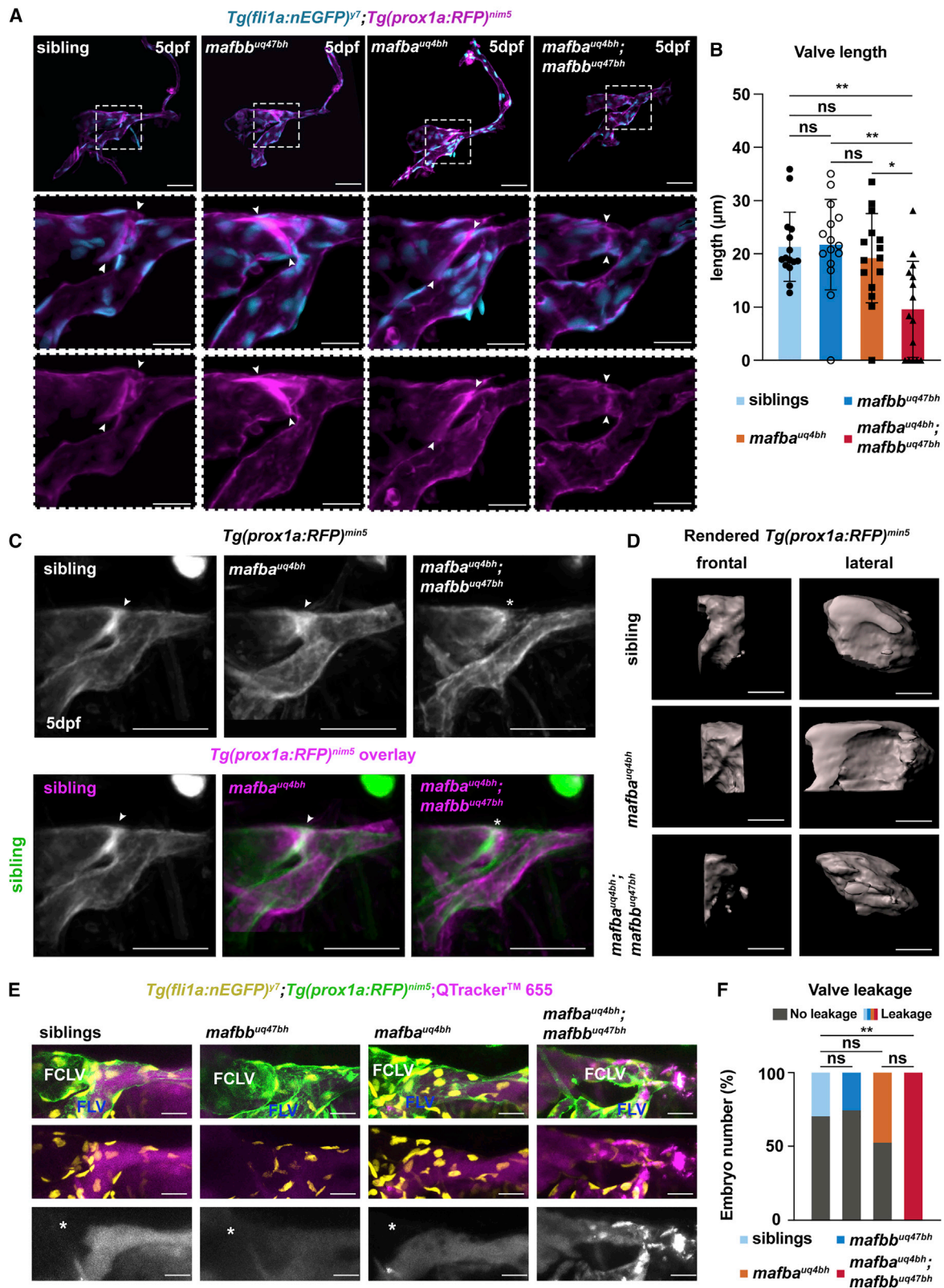
(E) Quantification of rendered surfaces. Embryos per genotype; n = 10. (left) Volume Kruskal-Wallis: ****p < 0.0001 for siblings versus double mutants; **p = 0.0079 for *mafbb* versus double mutants; *p = 0.045 for *mafba* versus double mutants; ns for all other comparisons p \geq 0.244. (Center) Area. One-way ANOVA: ****p < 0.0001 for siblings or *mafbb* versus double mutants; **p < 0.0025 for *mafba* versus double mutants; ns for all other comparisons p \geq 0.186. (Right) Sphericity. One-way ANOVA: ns p \geq 0.234.

(F) Uptake of FITC-dextran presented as a ratio of the average pixel value of z slices inside and outside the lymphatics. siblings n = 9, *mafbb* n = 9, *mafba* n = 9, and double mutants n = 8. Two-way ANOVA: from +30 min to +3 h post-FITC-dextran injection uptake is ****p < 0.0001 for siblings ***p = 0.0003 for *mafbb*, **p = 0.0014 for *mafba*, and ns p = 0.2415 for double mutants. +3 h post-FITC-dextran injection FITC-dextran uptake: *p = 0.0265 for siblings versus double mutants. Other interactions: ns p \geq 0.0626.

(G) Confocal projection of LFL with FITC-dextran (cyan) and *Tg(-5.2lyve1b:DsRed2)* (magenta) in siblings and double mutants at 5 dpf. Images of pre-injection, +30 min and +3 h post-injection. Scale bars, 100 μ m. White line: trajectory for graphs in (H).

(H) Fluorescence profile of *Tg(-5.2lyve1b:DsRed2)* (magenta) and FITC-dextran (cyan) intersecting the lymphatics from (G). ns, non-significant; stars are significant; error bars are mean \pm SD.

See also Figure S2 and Videos S1, S2, S3, and S4.



(legend on next page)

increase of embryos with leakage from the FLV to facial collecting lymphatic vessel (FCLV) in *mafba*;*mafbb* mutants compared with siblings (Figure 3F). These data suggest that *mafba* and *mafbb* are required for the formation and function of the valve in the facial lymphatics and that in their absence, lymph flow cannot be correctly channeled.

Topographical differences in Vegfc/d-SoxF downstream effectors during lymphatic-vessel formation

Recent reports have revealed differential requirements of Vegf ligands and receptors during lymphangiogenesis (Astin et al., 2014; Bower et al., 2017a, 2017b; Shin et al., 2016; Vogrin et al., 2019). We have previously shown that *mafba* expression is dependent on Vegfc-SoxF (Koltowska et al., 2015b). We hypothesize that *mafba* and *mafbb* also act downstream of the Vegf-SoxF axis. First, we confirmed that MO-*vegfc* and -*vegfd* recapitulate the published mutant phenotypes, while standard control MO did not induce lymphatic phenotypes (Figures S4A and S4B) (Astin et al., 2014; Hogan et al., 2009a, 2009b). We investigated the facial lymphatic phenotype in the previously published *sox7* and *sox18* mutants at 3 dpf, before the onset of significant edema due to PCV-DA shunts (Herpers et al., 2008) (Figure 4A). The single *sox7* or *sox18* mutants did not show lymphatic phenotypes, but *sox7*^{-/-}*sox18*^{-/-} and *sox7*^{-/-}*sox18*^{+/-} embryos showed a reduction in FLS (Figure 4A), recapitulating the *soxF* double morpholino phenotype (Figures S4A and S4B).

To uncover the potential direct regulators of *mafbb*, we investigated the presence of cis-regulatory elements (CREs). We identified conserved non-coding DNA sequences in the regions upstream and downstream of *mafbb* using mVista (Dubchak et al., 2000; Frazer et al., 2004; Mayor et al., 2000) and found a 151 bp conserved region 6 kbp downstream of *mafbb* (Figure S3A). This element is part of a previously described *mafbb* enhancer driving reporter expression in the venous and lymphatic endothelium at 55 hpf (Quillien et al., 2017). We generated a stable transgenic line, *Tg(mafbbE1bas:EGFP)*, which recapitulates endogenous *mafbb* expression (Figures S3C and S3D). We found no changes in the expression of *Tg(mafbbE1bas:EGFP)* in MO-*vegfc*, MO-*vegfd*, MO-*sox7*, MO-*sox18*, or double morpholino treatments (Figures 4B and S3F–S3I). We used

MEMESuite (Bailey et al., 2009) to identify conserved motifs in the *mafbb* CREs and found 10 predicted transcription-binding sites, none of them Sox7 or Sox18 (Figures S3B and S3E). Together, these observations suggest that this *mafbb* CRE is not regulated by SoxF.

To investigate *mafba* and *mafbb* expression in the facial lymphatics in response to Vegfc/d-SoxF signaling, we took a quantitative real-time PCR approach. We isolated LECs and venous endothelial cells (VECs) from dissected heads by sorting for cells double positive for *Tg(-5.2lyve1b:Venus)* and *Tg(fli1a:H2B-mCherry)* (Figure S4C) and found a trend of *mafba* and *mafbb* downregulation in the craniofacial VECs and LECs depleted of Vegfc-Vegfd signaling or SoxF (Figure S4D). Next, we determined if the level of expression of *mafba* and *mafbb* is downregulated specifically in LECs. We isolated facial LECs by sorting cells double positive for *Tg(prox1a:RFP)* and *Tg(fli1a:nEGFP)* from dissected heads (Figure S4C). We compared expression levels of *mafba* and *mafbb* in wild-type embryos and did not observe differences, confirming that both genes are present in developing LECs at similar levels (Figure 4C). We observed that *mafba* and *mafbb* expression is reduced in *vegfc* morphants and that there is a trend of reduced expression in *vegfd* and *vegfc-vegfd* morphants (Figures 4D and 4E). We found a significant difference in *mafbb*, but not *mafba*, expression in *sox7/18* morphants (Figures 4D and 4E). This revealed an unexpected difference in *mafba* and *mafbb* regulation in facial lymphatics downstream of Vegfc-Vegfd and SoxF. This shows that the two paralogs are differentially activated downstream of Vegf-SoxF signaling and that *mafbb* is constitutively expressed and regulated in facial LECs and is required for proper facial lymphatic formation.

mafba and *mafbb* are required for face LEC migration

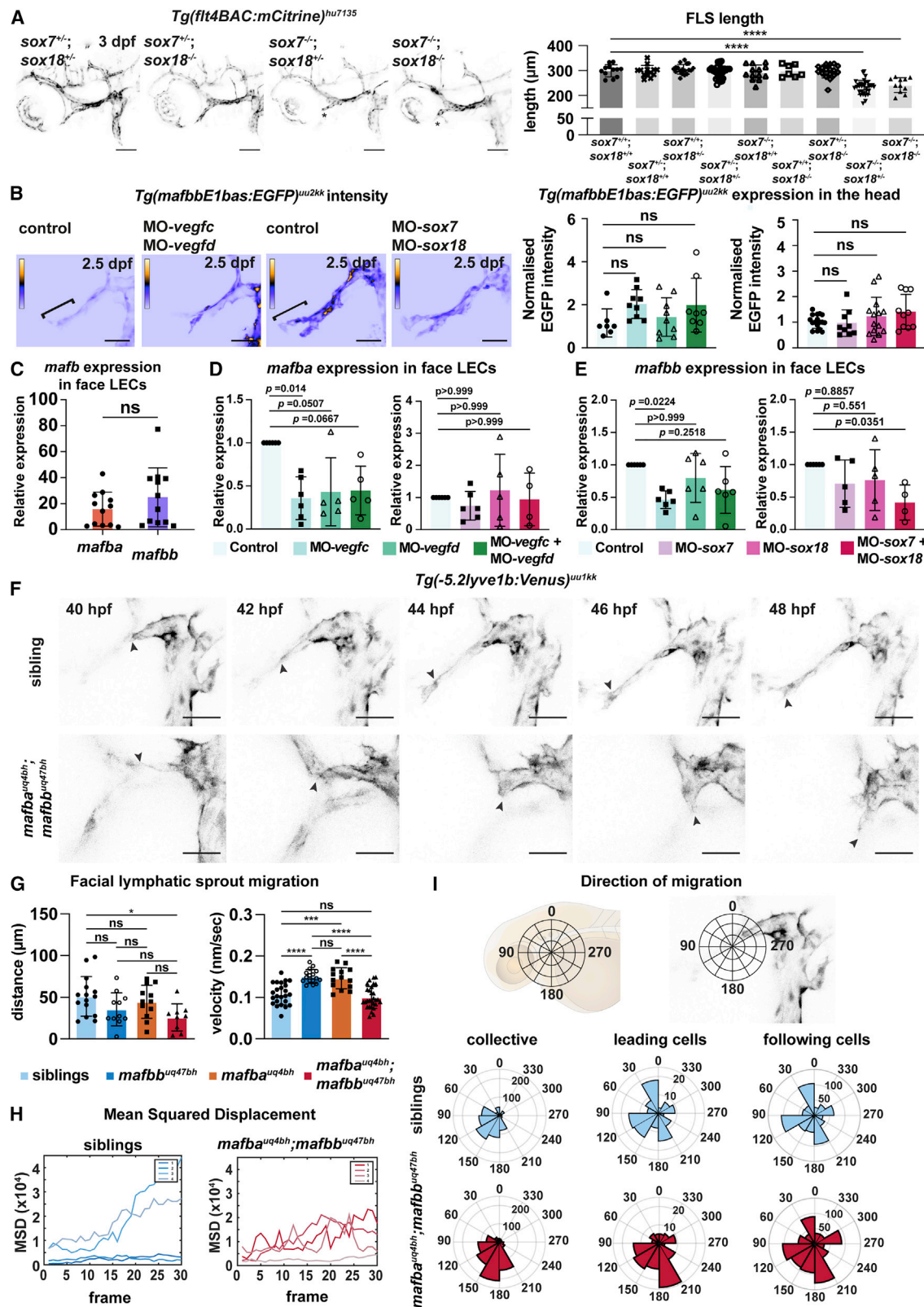
Our previous work has shown that *mafba* is essential for LEC migration in the trunk (Koltowska et al., 2015b). To identify if *mafba* and *mafbb* play a similar role in facial LEC migration, we used time-lapse imaging. By combining *Tg(-5.2lyve1b:Venus)* and *Tg(fli1a:H2B-mCherry)* transgenic lines, we documented in real-time the LEC trajectories in all genotypes.

From 40 hpf, we observed initial migration of the FLS from the CCV in an anterior-ventral direction (Figures 4F and S4E;

Figure 3. *mafba* and *mafbb* are required for valve formation and function in the facial lymphatics

- (A) Confocal projection of facial lymphatics and valve (arrowheads) labeled with *Tg(fli1a:nEGFP)* (cyan) and *Tg(prox1a:RFP)* (magenta) at 5 dpf, masked with surface rendering of both channels. Scale bars: 50 and 20 μ m. Dashed box: magnified images.
- (B) Valve-length measure from (A). Embryos per genotype; n = 15. Kruskal-Wallis test: **p \leq 0.009 for double mutants versus sibling or *mafbb*; *p = 0.044 *mafba* versus double mutants; other comparisons: ns p > 0.9999.
- (C) (Top) Projections of the average phenotype of siblings (n = 12), *mafba* mutants (n = 11), and double mutants (n = 12) in *Tg(prox1a:RFP)* embryos at 5dpf. Arrow: lymphatic valve; *: its absence. (Bottom) Overlay of siblings (green) with siblings and *mafba* or double mutants (magenta). Arrow: valve; *: absent valve. Scale bar, 50 μ m.
- (D) Surface rendering of *Tg(prox1a:RFP)* showing valve structure in siblings, *mafba* mutants, and double mutants at 5 dpf. Frontal and lateral views. Scale bar, 10 μ m.
- (E) Confocal imaging of *Tg(fli1a:nEGFP)* (yellow, endothelium), *Tg(prox1a:RFP)* (green), and Qtracker 665 (magenta) in the facial lymphatics at 5 dpf, in siblings and *mafbb*, *mafba*, and double mutants, 5 min post-injection. FCLV, facial collecting lymphatic valve; FLV, facial lymphatic vessel. *: absence of dye in FCLV. Scale bar, 50 μ m.
- (F) Percentage of embryos with dye leakage into FCLV at 5 min post-injection in siblings (n = 17), *mafbb* mutants (n = 8), *mafba* mutants (n = 15), and double mutants (n = 6). Chi-squared; p = 0.0159. Single comparisons with Fisher's exact test: **p \leq p = 0.009 for double mutants versus siblings or *mafbb*; *p = 0.0456 for *mafba* versus double mutants; other comparisons: ns with p \geq 0.399. ns, non-significant; stars are significant; error bars are mean \pm SD.

See also Figure S2 and Video S2.



(legend on next page)

Videos S3, S4, S5, and S6). Tracking the FLS migratory tip or individual cells, we found that in *mafba;mafbb* mutants, the FLS tip migratory distance was reduced compared with siblings, yet the FLS cells' velocity was not affected at 40–45 hpf (Figure 4G). In addition, there was no significant difference in the leading and following cells' velocity within the FLS in sibling and *mafba;mafbb* double mutants (Figure S4F), suggesting that cell motility was not affected. In siblings, the FLS tip advances over time, as revealed by the increasing or constant mean-squared displacement (MSD) (Figure 4H). However, in *mafba;mafbb* mutants, this value fluctuates, indicating that the tip progression rate is disrupted, resulting in stalling or changes in the migratory route (Figure 4H).

To establish if the migration defects are caused by an altered trajectory, we quantified cell-movement directionality (Figures 4I and S4H). In siblings, FLS cells collectively migrate in an anterior-ventral direction, predominantly between 120° and 150°, whereas this shifts ventrally to between 150° and 180° in *mafba;mafbb* double mutants (Figure 4I). To understand these directional differences, we separated leading cells from following cells and repeated the analysis. We observed that sibling leading cells are moving in various directions and sense their environment, with 0°–30°, 90°–150°, and 180°–210° being the most common cell-migration directions (Figure 4I). In *mafba;mafbb* double mutants, leading cells have instead a strong directional preference for the ventral-posterior direction (180°–210°) (Figure 4I), potentially due to loss of the ability to sense the environment. To further determine how the change of behavior in leading cells impacts the following LECs, we analyzed the followers' trajectory indices. We found that sibling following cells migrate toward 0°–30°, 90°–120°, and 180°–210°, while in mutants, the following-cell migration is more randomized. Further, while in siblings, the migratory direction of leading and following cells is remarkably similar, in

mafba;mafbb double mutants, leading and following LECs have different directional preferences (Figure 4I).

Overall, we see no significant difference in the migratory distance of the FLS or the directionality of collective cell migration in *mafba* or *mafbb* single mutants when compared with siblings (Figures 4G and S4H). In *mafba* mutants, the MSD is the same as for siblings (Figure S4G), while the direction of migration is disrupted in leading cells (Figure S4H), whereas the reverse is found in *mafbb* mutants where leading cells show the same directional preference as siblings (Figure S4H), but the MSD is similar to *mafba;mafbb* mutants (Figure S4G). In both *mafbb* and *mafba* single mutants, we see a significant increase in velocity (Figures 4G and S4F). As the vessel morphology and function are largely normal in these mutants, we speculate that the velocity increase ensures that the cells migrate the same distance. These data indicate that *mafba* and *mafbb* together are necessary for directional LEC migration.

In summary, we have found that facial lymphatic development differentially requires *Mafba* and *Mafbb* downstream of *Vegfc/d-SoxF* to promote the directionality of LEC migration. Ultimately, this work defined that *Mafbb* and *Mafba* are required to regulate LEC migration in the face, while *Mafba* alone regulates this process in the trunk. On the contrary, *muLECs* develop in a *Mafba*- and *Mafbb*-independent manner. This highlights the important differences in regulatory mechanisms driving lymphatic development across the zebrafish embryo. Together, our findings uncovered that selective transcription-factor combinatory levels drive lymphatic development in a topographically distinct manner. This spatially distinct regulation of lymphangiogenesis suggests that despite the highly conserved developmental programs in lymphatic development, progenitor niches present key differences in transcriptional code, which might change the way we view lymphatic-vessel development on a whole-organism level.

Figure 4. *mafba* and *mafbb* regulate facial LEC migration downstream of *Vegfc-Vegfd-SoxF*

- (A) (Left) Confocal images of *Tg(flt4BAC:mCitrine)* expression in facial lymphatics in sibling, *sox7^{+/+};sox18^{+/+}*, *sox7^{-/-};sox18^{+/+}*, and *sox7^{-/-};sox18^{-/-}* embryos at 3 dpf. *: reduced sprout length. Scale bars, 100 μ m. (Right) Quantification of facial lymphatic sprout length at 3 dpf in *sox7* and *sox18* mutant backgrounds. *sox7^{+/+};sox18^{+/+}* n = 12; *sox7^{+/+};sox18^{+/+}* and *sox7^{-/-};sox18^{+/+}* n = 13; *sox7^{+/+};sox18^{-/-}* n = 18; *sox7^{-/-};sox18^{+/+}* n = 30; *sox7^{+/+};sox18^{-/-}* n = 7; *sox7^{-/-};sox18^{-/-}* n = 17; *sox7^{-/-};sox18^{+/+}* n = 32; *sox7^{-/-};sox18^{-/-}* n = 11. One-way ANOVA: ****p < 0.0001 for *sox7^{+/+};sox18^{+/+}* versus *sox7^{-/-};sox18^{+/+}* or *sox7^{-/-};sox18^{-/-}*; other comparisons: p > 0.9782.
- (B) (Top) Heatmap of *Tg(mafbbE1bas:EGFP)* signal intensity from confocal projection at 2.5 dpf in face LECs. Gray value intensity scale: 0–113 for control and MO-*vegfc* + MO-*vegfd*, scale: 0–147 for control and MO-*sox7*+MO-*sox18*. White bracket: quantification area. Scale bar, 50 μ m. (Bottom) Quantification of *Tg(mafbbE1bas:EGFP)* intensity. (Left) Control n = 7; MO-*vegfd* and MO-*vegfc* n = 9; MO-*vegfc* + *vegfd* n = 8; (right) control n = 17; MO-*sox7* n = 9; MO-*sox18* n = 14; MO-*sox7* + *sox18* n = 10. Kruskal-Wallis test: ns p > 0.2372.
- (C) Quantitative real-time PCR of *mafba* and *mafbb* expression relative to *cdh5* in facial LECs at 48 hpf. 12 replicates. Wilcoxon test: ns p = 0.3013.
- (D and E) Quantitative real-time PCR of *mafba* and *mafbb* expression in face LECs at 48 hpf. (D, left) 6 replicates for control and MO-*vegfc* and 5 for MO-*vegfd* and MO-*vegfc* + *vegfd*; expression relative to *cdh5*. (D, right) 6 replicates for control, MO-*sox7*, 5 for MO-*sox18*, and 4 for MO-*sox7*+MO-*sox18*; expression relative to *B actin*. (E, left) 6 replicates for control, MO-*vegfd*, MO-*vegfc*, and MO-*vegfc* + *vegfd*; expression relative to *cdh5*. (E, right) 6 replicates for control, 5 for MO-*sox7* and MO-*sox18*, and 4 for MO-*sox7*+MO-*sox18*; expression relative to *B actin*. p values reported on the graph.
- (F) Confocal projections from time-lapse imaging of LEC migration in siblings and double mutants labeled by *Tg(-5.2lyve1b:Venus)* from 40–48 hpf. Arrows: leading cells in FLS. Scale bars, 50 μ m.
- (G) (Left) FLS migratory distance (from F). Embryos: siblings n = 15, *mafbb* n = 11, *mafba* n = 12; double mutants n = 9. One-way ANOVA: *p = 0.0279 for siblings versus double mutants; ns for all other comparisons. (Right) FLS migratory velocity (from F). Cells: siblings n = 24, *mafbb* n = 16, *mafba* n = 14; double mutants n = 29. One-way ANOVA: ****p < 0.0001 for siblings versus *mafbb*, and *mafbb* or *mafba* versus double mutants; ***p = 0.0001 for siblings versus *mafba*; ns for all other comparisons.
- (H) FLS tip mean-squared displacement (MSD) (from F) in siblings (n = 4) and double mutants (n = 4).
- (I) (Top) Schematic representation of directionality in the polar histograms. (Bottom) Polar histograms of migration tracked (from F) in siblings (n = 4) and double mutants (n = 4). Collective cells: siblings n = 24 and double mutants n = 29; leading cells: siblings n = 4 and double mutants n = 4; following cells: siblings n = 20 and double mutants n = 25. ns, non-significant; stars are significant; mean with SD.

See also Figures S3 and S4 and Videos S3, S4, S5, and S6.

Limitations of the study

Due to technical limitations, this study has not identified the mechanisms by which *mafba* and *mafbb* are differentially regulated directly downstream of VegF and SoxF signaling. It is also limited in the mechanistic insight by which *mafba* and *mafbb* regulate the direction of LEC migration. Future work is needed to further identify the direct downstream targets of Mafba and Mafbb, which orchestrate the cellular processes involved in shaping functional lymphatic vessels.

STAR★METHODS

Detailed methods are provided in the online version of this paper and include the following:

- **KEY RESOURCES TABLE**
- **RESOURCE AVAILABILITY**
 - Lead contact
 - Materials availability
 - Data and code availability
- **EXPERIMENTAL MODEL AND SUBJECT DETAILS**
- **METHOD DETAILS**
 - Mutant generation and identification
 - *mafbb* CRE identification
 - Generating a cis-regulatory transgenic line
 - Morpholino-mediated knockdown, genotyping and genome editing
 - Dye injections
 - Immunostaining
 - *In situ* hybridization
 - Image acquisition
 - VAST system imaging
 - Fluorescence-activated cell sorting (FACS) and gene expression analysis
- **QUANTIFICATION AND STATISTICAL ANALYSIS**
 - LEC number quantification
 - Image rendering
 - Lymphatic functional analysis
 - Fluorescent intensity quantification
 - Average image analysis
 - Cell migration analysis
 - Statistical analysis

SUPPLEMENTAL INFORMATION

Supplemental information can be found online at <https://doi.org/10.1016/j.celrep.2022.110982>.

ACKNOWLEDGMENTS

This work was supported by a Wallenberg Academy Fellowship (2017.0144), a Ragnar Söderbergs Fellowship (M13/17), Vetenskapsrådet (VR-MH-2016-01437), and the Jeansson Foundation. The Genome Engineering Zebrafish at SciLifeLab provided VAST and fragment-length analysis (FLA) services. Fluorescence-activated cell sorting (FACS) was performed at BioVis at Uppsala University. We would like to thank Neil Bower and Milena Doroszko for help with quantitative real-time PCR setup and Anna Klemm for the image-analysis support. P.R. and A.A. were funded via the BioImage Informatics Facility, a unit of the National Bioinformatics Infrastructure Sweden (NBIS), with funding from SciLifeLab, National Microscopy Infrastructure NMI (VR-RFI

2019-00217), and the Chan Zuckerberg Initiative. M.H. and S.S.-M. were supported by CRC1348 (DFG, project B08).

AUTHOR CONTRIBUTIONS

H.A., V.P., and K.K. conceptualized the project, performed experiments, analyzed data, and co-wrote the manuscript. M.H., B.F.-G., R.S., M.G., and S.S.-M. performed experiments and analyzed data. P.R. and A.A. analyzed experiments. B.H. provided unpublished reagents.

DECLARATION OF INTERESTS

The authors declare no competing interests.

Received: March 12, 2021

Revised: April 11, 2022

Accepted: May 27, 2022

Published: June 21, 2022

REFERENCES

- Aleström, P., D'Angelo, L., Midtlyng, P.J., Schorderet, D.F., Schulte-Merker, S., Sohm, F., and Warner, S. (2020). Zebrafish: housing and husbandry recommendations. *Lab. Anim.* 54, 213–224. <https://doi.org/10.1177/0023677219869037>.
- Allalou, A., Wu, Y., Ghannad-Rezaie, M., Eimon, P.M., and Yanik, M.F. (2017). Automated deep-phenotyping of the vertebrate brain. *Elife* 6, e23379. <https://doi.org/10.7554/eLife.23379>.
- Almstedt, E., Elgendy, R., Hekmati, N., Rosén, E., Wärn, C., Olsen, T.K., Dyberg, C., Doroszko, M., Larsson, I., Sundström, A.A., et al. (2020). Integrative discovery of treatments for high-risk neuroblastoma. *Nat. Commun.* 11, 71. <https://doi.org/10.1038/s41467-019-13817-8>.
- Astin, J.W., Haggerty, M.J.L., Okuda, K.S., Le Guen, L., Misa, J.P., Tromp, A., Hogan, B.M., Crosier, K.E., and Crosier, P.S. (2014). Vegfd can compensate for loss of Vegfc in zebrafish facial lymphatic sprouting. *Dev. Camb. Engl.* 141, 2680–2690. <https://doi.org/10.1242/dev.106591>.
- Baek, S., Oh, T.G., Secker, G., Sutton, D.L., Okuda, K.S., Paterson, S., Bower, N.I., Toubia, J., Koltowska, K., Capon, S.J., et al. (2019). The alternative splicing regulator Nova2 constrains vascular Erk signaling to limit specification of the lymphatic lineage. *Dev. Cell* 49, 279–292.e5. <https://doi.org/10.1016/j.devcel.2019.03.017>.
- Bailey, T.L., Boden, M., Buske, F.A., Frith, M., Grant, C.E., Clementi, L., Ren, J., Li, W.W., and Noble, W.S. (2009). MEME SUITE: tools for motif discovery and searching. *Nucleic Acids Res.* 37, W202–W208. <https://doi.org/10.1093/nar/gkp335>.
- Bower, N.I., Koltowska, K., Pichol-Thieuvend, C., Virshup, I., Paterson, S., Lagendijk, A.K., Wang, W., Lindsey, B.W., Bent, S.J., Baek, S., et al. (2017a). Mural lymphatic endothelial cells regulate meningeal angiogenesis in the zebrafish. *Nat. Neurosci.* 20, 774–783. <https://doi.org/10.1038/nn.4558>.
- Bower, N.I., Vogrin, A.J., Le Guen, L., Chen, H., Stacker, S.A., Achen, M.G., and Hogan, B.M. (2017b). Vegfd modulates both angiogenesis and lymphangiogenesis during zebrafish embryonic development. *Dev. Camb. Engl.* 144, 507–518. <https://doi.org/10.1242/dev.146969>.
- Brudno, M., Do, C.B., Cooper, G.M., Kim, M.F., Davydov, E., Program, N.C.S., Sidow, A., Batzoglou, S., and Batzoglou, S. (2003). LAGAN and Multi-LAGAN: Efficient tools for large-scale multiple alignment of genomic DNA. *Genome Res.* 13, 721–731. <https://doi.org/10.1101/gr.926603>.
- Carrington, B., Varshney, G.K., Burgess, S.M., and Sood, R. (2015). CRISPR-STAT: an easy and reliable PCR-based method to evaluate target-specific sgRNA activity. *Nucleic Acids Res.* 43, e157. <https://doi.org/10.1093/nar/gkv802>.
- Dieterich, L.C., Tacconi, C., Menzi, F., Proulx, S.T., Kapaklikaya, K., Hamada, M., Takahashi, S., and Detmar, M. (2020). Lymphatic MAFB regulates vascular patterning during developmental and pathological lymphangiogenesis. *Angiogenesis* 23, 411–423. <https://doi.org/10.1007/s10456-020-09721-1>.

- Dubchak, I., Brudno, M., Loots, G.G., Pachter, L., Mayor, C., Rubin, E.M., and Frazer, K.A. (2000). Active conservation of noncoding sequences revealed by three-way species comparisons. *Genome Res.* 10, 1304–1306. <https://doi.org/10.1101/gr.142200>.
- Dunworth, W.P., Cardona-Costa, J., Bozkulak, E.C., Kim, J.-D., Meadows, S., Fischer, J.C., Wang, Y., Cleaver, O., Qyang, Y., Ober, E.A., and Jin, S.-W. (2014). Bone Morphogenetic protein 2 signaling negatively modulates lymphatic development in vertebrate embryos. *Circ. Res.* 114, 56–66. <https://doi.org/10.1161/CIRCRESAHA.114.302452>.
- Eng, T.C.Y., Chen, W., Okuda, K.S., Misa, J.P., Padberg, Y., Crosier, K.E., Crosier, P.S., Hall, C.J., Schulte-Merker, S., Hogan, B.M., and Astin, J.W. (2019). Zebrafish facial lymphatics develop through sequential addition of venous and non-venous progenitors. *EMBO Rep.* 20, 1–17. <https://doi.org/10.15252/embr.201847079>.
- Frazer, K.A., Pachter, L., Poliakov, A., Rubin, E.M., and Dubchak, I. (2004). VISTA: computational tools for comparative genomics. *Nucleic Acids Res.* 32, W273–W279. <https://doi.org/10.1093/nar/gkh458>.
- Gagnon, J.A., Valen, E., Thyme, S.B., Huang, P., Ahkmetova, L., Pauli, A., Montague, T.G., Zimmerman, S., Richter, C., and Schier, A.F. (2014). Efficient mutagenesis by Cas9 protein-mediated oligonucleotide insertion and large-scale assessment of single-guide RNAs. *PLoS One* 9, e98186. <https://doi.org/10.1371/journal.pone.0098186>.
- Venero Galanternik, M., Castranova, D., Gore, A.V., Blewett, N.H., Jung, H.M., Stratman, A.N., Kirby, M.R., Iben, J., Miller, M.F., Kawakami, K., et al. (2017). A novel perivascular cell population in the zebrafish brain. *Elife* 6, e24369. <https://doi.org/10.7554/eLife.24369>.
- Gudmundsson, S., Wilbe, M., Filippek-Górniok, B., Molin, A.-M., Ekvall, S., Johansson, J., Allalou, A., Gylje, H., Kalscheuer, V.M., Ledin, J., et al. (2019). TAF1, associated with intellectual disability in humans, is essential for embryogenesis and regulates neurodevelopmental processes in zebrafish. *Sci. Rep.* 9, 10730. <https://doi.org/10.1038/s41598-019-46632-8>.
- Herpers, R., van de Kamp, E., Duckers, H.J., and Schulte-Merker, S. (2008). Redundant roles for Sox7 and Sox18 in arteriovenous specification in zebrafish. *Circ. Res.* 102, 12–15. <https://doi.org/10.1161/CIRCRESAHA.107.166066>.
- Hogan, B.M., Herpers, R., Witte, M., Heloterä, H., Alitalo, K., Duckers, H.J., and Schulte-Merker, S. (2009a). Vegfr/Flt4 signalling is suppressed by Dll4 in developing zebrafish intersegmental arteries. *Development* 136, 4001–4009. <https://doi.org/10.1242/dev.039990>.
- Hogan, B.M., Bos, F.L., Bussmann, J., Witte, M., Chi, N.C., Duckers, H.J., and Schulte-Merker, S. (2009b). Ccbe1 is required for embryonic lymphangiogenesis and venous sprouting. *Nat. Genet.* 41, 396–398. <https://doi.org/10.1038/ng.321>.
- Karaman, S., Leppänen, V.M., and Alitalo, K. (2018). Vascular endothelial growth factor signaling in development and disease. *Development* 145, dev151019. <https://doi.org/10.1242/dev.151019>.
- Karkkainen, M.J., Haiko, P., Sainio, K., Partanen, J., Taipale, J., Petrova, T.V., Jeltsch, M., Jackson, D.G., Talikka, M., Rauvala, H., et al. (2004). Vascular endothelial growth factor C is required for sprouting of the first lymphatic vessels from embryonic veins. *Nat. Immunol.* 5, 74–80. <https://doi.org/10.1038/ni1013>.
- Kartopawiro, J., Bower, N.I., Karnezis, T., Kazenwadel, J., Betterman, K.L., Lesieur, E., Koltowska, K., Astin, J., Crosier, P., Vermeren, S., et al. (2014). Arap3 is dysregulated in a mouse model of hypotrichosis–lymphedema–telangiectasia and regulates lymphatic vascular development. *Hum. Mol. Genet.* 23, 1286–1297. <https://doi.org/10.1093/hmg/ddt518>.
- Klein, S., Staring, M., Murphy, K., Viergever, M.A., and Pluim, J. (2010). elastix: a toolbox for intensity-based medical image registration. *IEEE Trans. Med. Imaging* 29, 196–205. <https://doi.org/10.1109/TMI.2009.2035616>.
- Klotz, L., Norman, S., Vieira, J.M., Masters, M., Rohling, M., Dubé, K.N., Bollini, S., Matsuzaki, F., Carr, C.A., and Riley, P.R. (2015). Cardiac lymphatics are heterogeneous in origin and respond to injury. *Nature* 522, 62–67. <https://doi.org/10.1038/nature14483>.
- Koltowska, K., Betterman, K.L., Harvey, N.L., and Hogan, B.M. (2013). Getting out and about: the emergence and morphogenesis of the vertebrate lymphatic vasculature. *Development* 140, 1857–1870. <https://doi.org/10.1242/dev.089565>.
- Koltowska, K., Lagendijk, A.K., Pichol-Thieuvend, C., Fischer, J.C., Francois, M., Ober, E.A., Yap, A.S., and Hogan, B.M. (2015a). Vegf regulates bipotential precursor division and Prox1 expression to promote lymphatic identity in zebrafish. *Cell Rep.* 13, 1828–1841. <https://doi.org/10.1016/j.celrep.2015.10.055>.
- Koltowska, K., Okuda, K.S., Gloger, M., Rondon-Galeano, M., Mason, E., Xuan, J., Dudczig, S., Chen, H., Arnold, H., Skoczylas, R., et al. (2021). The RNA helicase Ddx21 controls Vegf-driven developmental lymphangiogenesis by balancing endothelial cell ribosome biogenesis and p53 function. *Nat. Cell Biol.* 23, 1136–1147. <https://doi.org/10.1038/s41556-021-00784-w>.
- Koltowska, K., Paterson, S., Bower, N.I., Baillie, G.J., Lagendijk, A.K., Astin, J.W., Chen, H., Francois, M., Crosier, P.S., Taft, R.J., et al. (2015b). Mafba is a downstream transcriptional effector of vegf signaling essential for embryonic lymphangiogenesis in zebrafish. *Genes Dev.* 29, 1618–1630. <https://doi.org/10.1101/gad.263210.115>.
- Küchler, A.M., Gjini, E., Peterson-Maduro, J., Cancilla, B., Wolburg, H., and Schulte-Merker, S. (2006). Development of the zebrafish lymphatic system requires vegf signaling. *Curr. Biol.* 16, 1244–1248. <https://doi.org/10.1016/j.cub.2006.05.026>.
- Lawson, N.D., and Weinstein, B.M. (2002). *In vivo* imaging of embryonic vascular development using transgenic zebrafish. *Dev. Biol.* 248, 307–318. <https://doi.org/10.1006/dbio.2002.0711>.
- Le Guen, L., Karpanen, T., Schulte, D., Harris, N.C., Koltowska, K., Roukens, G., Bower, N.I., van Impel, A., Stacker, S.A., Achen, M.G., et al. (2014). Ccbe1 regulates Vegf-mediated induction of Vegfr3 signaling during embryonic lymphangiogenesis. *Development* 141, 1239–1249. <https://doi.org/10.1242/dev.100495>.
- Martinez-Corral, I., Ulvmar, M.H., Stanczuk, L., Tatin, F., Kizhatil, K., John, S.W.M., Alitalo, K., Ortega, S., and Makinen, T. (2015). Nonvenous origin of dermal lymphatic vasculature. *Circ. Res.* 116, 1649–1654. <https://doi.org/10.1161/CIRCRESAHA.116.306170>.
- Mayor, C., Brudno, M., Schwartz, J.R., Poliakov, A., Rubin, E.M., Frazer, K.A., Pachter, L.S., and Dubchak, I. (2000). Vista: visualizing global DNA sequence alignments of arbitrary length. *Bioinformatics* 16, 1046–1047. <https://doi.org/10.1093/bioinformatics/16.11.1046>.
- Okuda, K.S., Astin, J.W., Misa, J.P., Flores, M.V., Crosier, K.E., and Crosier, P.S. (2012). Lyve1 expression reveals novel lymphatic vessels and new mechanisms for lymphatic vessel development in zebrafish. *Dev. Camb.* 139, 2381–2391. <https://doi.org/10.1242/dev.077701>.
- Pichol-Thieuvend, C., Betterman, K.L., Liu, X., Ma, W., Skoczylas, R., Lesieur, E., Bos, F.L., Schulte, D., Schulte-Merker, S., Hogan, B.M., et al. (2018). A blood capillary plexus-derived population of progenitor cells contributes to genesis of the dermal lymphatic vasculature during embryonic development. *Dev. Camb.* 145, dev160184. <https://doi.org/10.1242/dev.160184>.
- Quillien, A., Abdalla, M., Yu, J., Ou, J., Zhu, L.J., and Lawson, N.D. (2017). Robust identification of developmentally active endothelial enhancers in zebrafish using FANS-assisted ATAC-seq. *Cell Rep.* 20, 709–720. <https://doi.org/10.1016/j.celrep.2017.06.070>.
- Rohlfing, T., Brandt, R., Maurer, C.R., and Menzel, R. (2001). Bee brains, B-splines and computational democracy: generating an average shape atlas. In *Proceedings IEEE Workshop on Mathematical Methods in Biomedical Image Analysis (MMBIA 2001)*, pp. 187–194. <https://doi.org/10.1109/MMBIA.2001.991733>.
- Rondon-Galeano, M., Skoczylas, R., Bower, N.I., Simons, C., Gordon, E., Francois, M., Koltowska, K., and Hogan, B.M. (2020). MAFB modulates the maturation of lymphatic vascular networks in mice. *Dev. Dyn.* 249, 1201–1216. <https://doi.org/10.1002/dvdy.209>.
- Schindelin, J., Arganda-Carreras, I., Frise, E., Kaynig, V., Longair, M., Pietzsch, T., Preibisch, S., Rueden, C., Saalfeld, S., Schmid, B., et al. (2012). Fiji: an

- open-source platform for biological-image analysis. *Nat. Methods* 9, 676–682. <https://doi.org/10.1038/nmeth.2019>.
- Schneider, C.A., Rasband, W.S., and Eliceiri, K.W. (2012). NIH Image to ImageJ: 25 years of image analysis. *Nat. Methods* 9, 671–675. <https://doi.org/10.1038/nmeth.2089>.
- Shin, M., Male, I., Beane, T.J., Villefranc, J.A., Kok, F.O., Zhu, L.J., and Lawson, N.D. (2016). Vegfc acts through ERK to induce sprouting and differentiation of trunk lymphatic progenitors. *Dev. Camb. Engl.* 143, 3785–3795. <https://doi.org/10.1242/dev.137901>.
- Shin, M., Nozaki, T., Idrizi, F., Isogai, S., Ogasawara, K., Ishida, K., Yuge, S., Roscoe, B., Wolfe, S.A., Fukuhara, S., et al. (2019). Valves are a conserved feature of the zebrafish lymphatic system. *Dev. Cell* 51, 374–386.e5. <https://doi.org/10.1016/j.devcel.2019.08.019>.
- Stanczuk, L., Martinez-Corral, I., Ulmar, M.H., Zhang, Y., Laviña, B., Fruttiger, M., Adams, R.H., Saur, D., Betsholtz, C., Ortega, S., et al. (2015). cKit lineage hemogenic endothelium-derived cells contribute to mesenteric lymphatic vessels. *Cell Rep.* 10, 1708–1721. <https://doi.org/10.1016/j.celrep.2015.02.026>.
- van Impel, A., Zhao, Z., Hermkens, D.M.A., Roukens, M.G., Fischer, J.C., Petteerson-Maduro, J., Duckers, H., Ober, E.A., Ingham, P.W., and Schulte-Merker, S. (2014). Divergence of zebrafish and mouse lymphatic cell fate specification pathways. *Development* 141, 1228–1238. <https://doi.org/10.1242/dev.105031>.
- van Lessen, M., Shibata-Germanos, S., van Impel, A., Hawkins, T.A., Rihel, J., and Schulte-Merker, S. (2017). Intracellular uptake of macromolecules by brain lymphatic endothelial cells during zebrafish embryonic development. *Elife* 6, e25932. <https://doi.org/10.7554/eLife.25932>.
- Vogrin, A.J., Bower, N.I., Gunzburg, M.J., Roufail, S., Okuda, K.S., Paterson, S., Headey, S.J., Stacker, S.A., Hogan, B.M., and Achen, M.G. (2019). Evolutionary differences in the vegf/vegfr code reveal organotypic roles for the endothelial cell receptor kdr in developmental lymphangiogenesis. *Cell Rep.* 28, 2023–2036.e4. <https://doi.org/10.1016/j.celrep.2019.07.055>.
- Wigle, J.T., and Oliver, G. (1999). Prox1 function is required for the development of the murine lymphatic system. *Cell* 98, 769–778. [https://doi.org/10.1016/S0092-8674\(00\)81511-1](https://doi.org/10.1016/S0092-8674(00)81511-1).
- Yaniv, K., Isogai, S., Castranova, D., Dye, L., Hitomi, J., and Weinstein, B.M. (2006). Live imaging of lymphatic development in the zebrafish. *Nat. Med.* 12, 711–716. <https://doi.org/10.1038/nm1427>.

STAR★METHODS

KEY RESOURCES TABLE

REAGENT or RESOURCE	SOURCE	IDENTIFIER
Antibodies		
Rabbit anti-Prox1 (1:500)	AngioBio Co	Cat# 11-002P, RRID:AB_10013720
chicken anti-GFP (1:400)	Abcam	Cat# ab13970, RRID:AB_300798
α -rabbit IgG-HRP (1:1000)	Cell Signalling	Cat# 7074, RRID:AB_2099233
goat α -rabbit Alexa Fluor 488 (1:200)	Thermo Fisher	Cat# A-11008, RRID:AB_143165
Click-iT® RNA Alexa Fluor®594 (1:500)	Thermo Fisher	Cat# C-10330
Chemicals, peptides, and recombinant proteins		
FITC-Dextran 10 kDa MW	Sigma	Cat# HY-128868
Qtracker™ 655 Vascular labels	Thermo Fisher	Cat# Q21021MP
5-ethynyl-2'-deoxyuridine (EdU)	Sigma	Cat# 900584
Critical commercial assays		
TSA™ Plus Cyanine 3 System	Perkin Elmer	Cat# NEL744001KT
MAXIscript T7 Transcription Kit	Invitrogen	Cat# AM1312
Click-iT™ RNA Alexa Fluor™ 594 Imaging Kit	Thermo Fisher	Cat# C10330
Quick-RNA Microprep kit	Cambridge Bioscience	Cat# R1050
SuperScript™ VILO™ cDNA Synthesis Kit	Thermo Fisher	Cat# 11754050
SsoAdvanced™ PreAmp Supermix	Bio-Rad	Cat# 1725160
Experimental models: Organisms/strains		
Zebrafish: <i>mafba</i> ^{uq4bh}	Koltowska et al., 2015b	ZDB-ALT-151231-5
Zebrafish: <i>mafbb</i> ^{uq47bh}	This paper	To be registered
Zebrafish: <i>Tg(fli1a:nEGFP)</i> ^{y7}	Lawson and Weinstein, 2002	ZFIN ID: ZDB-TGCONSTRUCT-070117-152
Zebrafish: <i>Tg(-5.2lyve1b:DsRed2)</i> ^{nz101}	Okuda et al., 2012	ZFIN ID: ZDB-TGCONSTRUCT-120723-4
Zebrafish: <i>TgBAC(prox1a:KaTA4-4xUAS-ADV.E1b:TagRFP)</i> ^{nim5}	Dunworth et al., 2014; van Impel et al., 2014	ZDB-TGCONSTRUCT-140521-2
Zebrafish: <i>Tg(kdr-l:ras-Cherry)</i> ^{s916}	Hogan et al., 2009a, 2009b	ZDB-ALT-090506-2
Zebrafish: <i>Tg(flt4BAC:mCitrine)</i> ^{hu7135}	van Impel et al., 2014	ZDB-TGCONSTRUCT-140521-1
Zebrafish: <i>Tg(fli1a:H2B-mCherry)</i> ^{uq37bh}	Baek et al., 2019	ZFIN_ZDB-ALT-191011-5
Zebrafish: <i>Tg(-5.2lyve1b:Venus)</i> ^{uu1kk}	This paper	To be registered
Zebrafish: <i>Tg(mafbbE1bas:EGFP)</i> ^{uu2kk}	This paper	To be registered
Plasmid: pT2-cryR;mafbbCE1-basEgfp	Quillien et al., 2017	Addgene Plasmid #90137
Oligonucleotides		
<i>mafbb</i> CRISPR gRNA primer (target site in capitals): 5' taatacgactcactat aGGCGAGCCTGGCGACGCAGG gtttagagctagaa3'	IDT/This paper	N/A
<i>mafbb</i> FLA genotyping primer Forward: 5' CTAAGCAGAAACGTCGTACC3'	IDT/This paper	N/A
<i>mafbb</i> FLA genotyping primer Reverse: 5' ACCACTAGCCTTTGCACT3'	IDT/This paper	N/A
KASP genotyping primer <i>mafba</i> ^{uq4bh} : 5'GGCCACGCGCAGCAA[C/T]AG CAGCAGCAGCAGC3'	LGC Biosearch Technologies/This paper	N/A

(Continued on next page)

Continued

REAGENT or RESOURCE	SOURCE	IDENTIFIER
KASP genotyping primer <i>mafba</i> ^{uq47bh} : 5'GAGC TCAACCGACATCTCCGCGGGATGAGCAAG GACGATATTATCCGCCTCAAGCAGAAACGTC GTACCTTAAAAAACCGCGGTACGCGCAGTC GTGTGGGCATAAACGCGTTTCAGCAGAAGCA CTTGCTGGAGCACGAGAAGACGAGCCTGGC GA[CGCAGGTGGA]GCAGCTGAAGCACGAG CTCGGTGGGTGGTGCAGAGAGAGACGC ATATAAATCAAGTGCAGAAAGGCTAGTGGTC GGAATGAGCTGCCAGAGCAATAATGGACC CTCTTGTGAAAACCCATCATCGCCCGAA3'	LGC Biosearch Technologies/This paper	N/A
Morpholino: MO- <i>vegfc</i> SB ATGCTC CTGCTGAGACACAGACAAG (4 µg/µl)	Gene Tools/ Astin et al., 2014	N/A
Morpholino: MO- <i>vegfc</i> TB GAAAATC CAAATAAGTGCAATTTAG (5 µg/µl)	Gene Tools/ Hogan et al., 2009a, 2009b	N/A
Morpholino: MO- <i>vegfd</i> CAAATGAAT CCGATACTGACCTGTT (8 µg/µl)	Gene Tools/ Astin et al., 2014	N/A
Morpholino: MO- <i>vegfc</i> + MO- <i>vegfd</i> GAA AATCCAAATAAGTGCAATTTAG + CAAATG AATCCGATACTGACCTGTT (2.5 µg/µl + 4 µg/µl)	Gene Tools/ Astin et al., 2014 , Hogan et al., 2009a, 2009b	N/A
Morpholino: MO- <i>sox7</i> CGCACTTA TCAGAGCCGCCATGTGC (5 µg/µl)	Gene Tools/ Herpers et al., 2008	N/A
Morpholino: MO- <i>sox18</i> ATATTCATTC CAGCAAGACCAACAC (5 µg/µl)	Gene Tools/ Herpers et al., 2008	N/A
Morpholino: MO- <i>sox7</i> + MO- <i>sox18</i> CGCAC TTATCAGAGCCGCCATGTGC + ATATTCAT TCCAGCAAGACCAACAC (2.5g µg/µl + 2.5 µg/µl)	Gene Tools/ Herpers et al., 2008	N/A
In-Fusion cloning primer <i>mafbb</i> Forward: 5'TGC AGG ATC CCA TCG ATA TGT CGG CGG AGC AGC AC3'		N/A
In-Fusion cloning primer <i>mafbb</i> Reverse: 5' GTT CTA GAG GCT CGA GCT ATC GCA AAT ATT CGG GC3'		N/A
RT-qPCR primer <i>mafbb</i> Forward: 5'CCCTGAGTTTGCGCACGGTA3'	IDT/This paper	N/A
RT-qPCR primer <i>mafbb</i> Reverse: 5'TGGACACAAGCTGCTGGTCG3'	IDT/This paper	N/A
RT-qPCR primer <i>cdh5</i> Forward: 5'AAGCCCAATGGTGACCTAAT3'	IDT/ Koltowska et al., 2015b	N/A
RT-qPCR primer <i>cdh5</i> Reverse: 5'ATGGTAACAACGGTAGTGGC3'	IDT/ Koltowska et al., 2015b	N/A
RT-qPCR primer <i>kdr1</i> Forward: 5'CTGGTGGAGAGGCTAGGAGA3'	IDT/ Koltowska et al., 2015b	N/A
RT-qPCR primer <i>kdr1</i> Reverse: 5'TGATCGGGATGTAGTCTTTC3'	IDT/ Koltowska et al., 2015b	N/A
Software and algorithms		
ImageJ	Schneider et al., 2012	https://imagej.nih.gov/ij/
Imaris 9.3.0	Oxford Instruments	N/A
MATLAB	MathWorks	N/A
Prism9	Graph Pad Software Inc.	N/A
Average image overlay analysis code	Allalou et al., 2017	https://github.com/aallalou/OPT-InSitu-Toolbox
Cell migration analysis code	This paper	https://zenodo.org/badge/latestdoi/288939338

RESOURCE AVAILABILITY

Lead contact

Further information and requests for resources and reagents should be directed to and will be fulfilled by the lead contact, Katarzyna Koltowska (kaska.koltowska@igp.uu.se).

Materials availability

Transgenic lines, gRNA primers and RT-qPCR primers will be made available on request.

Data and code availability

Custom code written for this project has been made available on GitHub and is publicly available. The DOI and URL for the GitHub repository can be found in the [Key resources table](#). Further information required to reanalyse the data generated in this paper is available from the [lead contact](#) upon request.

EXPERIMENTAL MODEL AND SUBJECT DETAILS

Zebrafish work was carried out under ethical approval from the Swedish Board of Agriculture (5.8.18–10590/2018). Zebrafish were housed at the Genome Engineering Zebrafish National Facility (SciLifeLab, Uppsala Sweden) and adults and embryos were housed according to the standard laboratory procedure ([Aleström et al., 2020](#)). At 24 hpf embryos were transferred to 200 μM 1-phenyl 2-thiourea for imaging. Published zebrafish lines used were *Tg(fli1a:nEGFP)^{y7}* ([Lawson and Weinstein, 2002](#)), *Tg(-5.2lyve1b:DsRed2)^{nz101}* ([Okuda et al., 2012](#)), *TgBAC(prox1a:KalTA4-4xUAS-ADV.E1b:TagRFP)^{nim5}* ([Dunworth et al., 2014](#); [van Impel et al., 2014](#)), *Tg(kdr-l:ras-Cherry)^{s916}* ([Hogan et al., 2009a; 2009b](#)), *Tg(fit4BAC:mCitrine)^{hu7135}* ([van Impel et al., 2014](#)) and *Tg(fli1a:H2B-mCherry)^{uq37bh}* ([Baek et al., 2019](#)). The transgenic lines *Tg(-5.2lyve1b:Venus)^{uu1kk}* and *Tg(mafbbE1bas:EGFP)^{uu2kk}* were generated for this study.

METHOD DETAILS

Mutant generation and identification

mafbb mutants were generated by CRISPR/Cas9 genome editing as described in [Gagnon et al. \(2014\)](#). The guide was designed in the BRLZ domain of *mafbb*. Zebrafish embryos were injected at one cell stage with the 70–140 ng/μL gRNA and 200 ng/μL Cas9 mRNA. Founder identification was carried out by Fragment Length Analysis (FLA) as described ([Carrington et al., 2015](#)). Primers used to generate guides and for FLA are listed in the [Key resources table](#) (the target site of the gRNA can be found in capitals for *mafbb_g21* primer).

Genotyping for *mafba^{uq4bh}* and *mafbb^{uq47bh}* was carried out using KASP assay according to the manufacturer's instructions (LGC Biosearch Technologies) and using a OneStepPlus Real-Time PCR System (Thermo Fisher). Primers used are listed in the [Key resources table](#).

mafbb CRE identification

Actinopterygian sequences of the complete upstream and downstream non-coding regions of *mafbb* were aligned using the LAGAN alignment program ([Brudno et al., 2003](#)) and peaks of conservation were identified using mVISTA ([Dubchak et al., 2000](#); [Frazer et al., 2004](#); [Mayor et al., 2000](#)).

Generating a cis-regulatory transgenic line

We established the transgenic line *Tg(mafbbE1bas:EGFP)^{uu2kk}* by injecting the construct pT2-cryR;mafbbCE1-basEgfp (Addgene plasmid #90137), at 20 ng/μL with 100 ng/μL tol2 transposase mRNA into the cell of wild type zebrafish embryos at the one-cell stage.

Morpholino-mediated knockdown, genotyping and genome editing

Morpholinos (MOs) used have been previously published: MO-vegfc and MO-vegfd by ([Astin et al., 2014](#)), MO-sox7 and MO-sox18 by ([Herpers et al., 2008](#)). Standard control morpholino (Gene Tools) was used to test toxicity. 1 nL of MO solutions were injected into the yolk at the one-cell stage. The MO-vegfcSB has been used in the RT-qPCR experiment, while the MO-vegfcT was used for the intensity quantifications. Details of each MO are listed in the [Key resources table](#).

Dye injections

For functional experiments embryos were injected with 1 nL of 5 mg/mL FITC-dextran 10 kDa MW (Sigma) in 0.2 M KCl in ventral to the facial lymphatics. Embryos were imaged on a Leica TCS SP8 DLS microscope 30 min and 3 h post-injection. Embryos were also injected with 1 nL of QtrackerTM 655 Vascular labels (Thermo Fisher) at 5 dpf into the region dorsal and ventral to the LFL for uptake experiments and imaged on a Leica TCS SP8 DLS microscope 3 h post-injection.

Embryos anaesthetised with Tricane were injected with 1 nL of Qtracker™ 655 Vascular labels (Thermo Fisher) at 5 dpf in the FLV for leakage experiments and imaged on a Leica TCS SP8 DLS microscope immediately post-injection, approximately 5 min post-injection a Leica TCS SP8 DLS microscope.

Immunostaining

Prox1 and GFP were detected by immunofluorescence staining as previously described (Le Guen et al., 2014; Shin et al., 2016), with the addition of a 25 min Proteinase K treatment at RT as described in (Koltowska et al., 2015b). To view 5-ethynyl-2'-deoxyuridine (EdU) incorporation into newly synthesised DNA we followed the method previously described in (Koltowska et al., 2021), with the adaptation that embryos were treated in EdU at 54 hpf and fixed at 56 hpf. *Tg(-5.2lyve1b:Venus)^{uu1kk}* staining was carried out using the method described above. The details of the antibodies used are listed in the [Key resources table](#).

In situ hybridization

The coding region of *mafbb* was cloned by In-Fusion® HD Cloning (Takara Bio) using the primers listed in the [Key resources table](#) into a PCS2+ vector linearized with XbaI and EcoRI. The probe was synthesised using the MAXIscript T7 Transcription Kit (Invitrogen) on the vector after linearization with BbvCI. Primers for probe synthesis can be found in the [Key resources table](#). *In situ* hybridization against *mafbb* was performed as previously described (Kartopawiro et al., 2014). For imaging, embryos were embedded in 8% agarose and sectioned in a Microm HM 650V microtome (Thermo-Fisher) with a slice thickness of 60 μm. Sections were mounted in Mowiol and imaged on a DMI8 Leica microscope with a N Plan L 20× objective (Leica).

Image acquisition

Transgenic fluorescent embryos were mounted laterally in 1% low-melting agarose and imaged in the face or trunk using a Leica TCS SP8 DLS microscope. The following objectives were used: Fluotar VISR 25× water objective (objective number: 11506375), HC PL APO CS2 40× water objective (objective number: 11506360) and HC PL Fluotar 20× dry objective (objective number: 11506519). For time-lapse imaging, embryos were imaged overnight from 40 hpf acquiring a frame approximately every 10 min. Brightfield images were taken using a Leica Fluorescent Stereo Microscope M165 FC and 1× objective (objective number: 10450028). Embryos were mounted in 3% methylcellulose. Images were processed using ImageJ 2.0.0 (Schindelin et al., 2012).

VAST system imaging

mafba^{uq4bh}, *mafbb^{uq47bh}*, *mafba^{uq4bh};mafbb^{uq47bh}* and sibling embryos were imaged at 5 dpf using the Vertebrate Automated Screening Technology (VAST) system (Almstedt et al., 2020; Gudmundsson et al., 2019). Fluorescent images of the facial lymphatics, muLECs loops and trunk lymphatics were acquired using the *Tg(-5.2lyve1b:DsRed2)^{nz101}* line and used in the quantifications in [Figure S1G](#).

Fluorescence-activated cell sorting (FACS) and gene expression analysis

Whole embryos were harvested at 3 dpf from an incross of *mafba^{+/uq4bh};mafbb^{+/+}*, or *mafba^{+/uq4bh};mafbb^{uq47bh/uq47bh}*, and selected based on phenotype. Embryos were harvested at 48 hpf and the heads were dissected by making an incision posterior of the otolithic vesicle. Isolation of cells was performed as previously described (Kartopawiro et al., 2014). Double positive cells were sorted for either transgenes *Tg(prox1a:RFP)^{nim5}* and *Tg(fli1a:nEGFP)^{y7}*, or *Tg(-5.2lyve1b:Venus)^{uu1kk}* and *Tg(fli1a:H2B-mCherry)^{uq37bh}* directly into 300 μL TRIzol™ LS Reagent (Thermo Fisher). RNA was extracted using the Quick-RNA Microprep kit (Cambridge Bioscience) according to manufacturers' instructions. cDNA synthesis was performed with the SuperScript™ VILO™ cDNA Synthesis Kit (Thermo Fisher) according to manufacturer's instructions with a longer incubation at 42°C of 120 min cDNA was amplified using the SsoAdvanced™ PreAmp Supermix (Bio-Rad) according to manufacturer instructions. Each sample was amplified in two replicates. RT-qPCR was carried out using the SsoAdvanced Universal SYBR Green Supermix (Bio-Rad) according to manufacturer's instructions on CFX384 Touch Real-Time PCR Detection System (Bio-Rad). Data were analysed using the CFX Maestro Software (Bio-Rad). Changes in gene expression were calculated relative to the expression of a control gene, and normalized to the corresponding controls. Primers are listed in the [Key resources table](#).

QUANTIFICATION AND STATISTICAL ANALYSIS

LEC number quantification

Image quantification was performed using z-stacks and manual counting in ImageJ 2.0.0. For LECs at 5 dpf, double-positive cells for *Tg(-5.2lyve1b:DsRed2)^{nz101}* and *Tg(fli1a:nEGFP)^{y7}* in face and trunk lymphatic vessels were scored. For LEC specification at 2 dpf double-positive cells for Prox1 and *Tg(fli1a:nEGFP)^{y7}* we scored. For image representation, trunk images were rendered using Imaris v9.3.0 with a surface detail of 1 μm for *Tg(fli1a:nEGFP)^{y7}*. Both channels, for *Tg(fli1a:nEGFP)^{y7}* and for Prox1, were then masked and these channels used for representative images. Final images were processed using ImageJ 2.0.0 for both face and trunk.

Image rendering

For volume, area and sphericity quantifications, surface rendering of the *Tg(-5.2lyve1b:DsRed2)^{nz101}* channel was carried out using Imaris v9.3.0. Surfaces were rendered with a surface detail of 2 μm , and vessels that were not part of the facial lymphatic network were removed (Figure 2D). Measurements were acquired using the statistics tool.

Valve surface rendering of *Tg(prox1a:RFP)^{nm5}* was carried out using Imaris v9.3.0. Surfaces were rendered with a surface detail of 0.1 μm , and the valve region extracted from the vessel (Figure 3D).

Lymphatic functional analysis

The lymphatic function analysis by dextran uptake was measured as a ratio of inside:outside average pixel value of the LFL. Image analysis was carried out using ImageJ 2.0.0. ROIs were drawn on individual z-slices which included the main vessel of the LFL (inside) or ventral to the LFL (outside), using the *Tg(-5.2lyve1b:DsRed2)^{nz101}* channel. The average pixel value was then taken for the FITC-dextran channel for the ROI on each z-slice and the mean pixel value was calculated across the z-slices, which varied between 5–9 slices depending on the thickness of the vessel. The average pixel value at 30 min and 3 h post-injection was normalised to the level from before FITC-dextran injection by taking the average of the z-slices of the LFL. To visualise the FITC-dextran distribution of the images in Figure 3G, a fluorescent profile was taken through the LFL at the anterior branching point in a z-stack of the slices spanning the LFL. A line was drawn intersecting the LFL and including the region dorsal and ventral to the LFL. The grey values for FITC-dextran and *Tg(-5.2lyve1b:DsRed2)^{nz101}* were plotted against the position along the line to show the relationship between the LFL and dextran absorbance.

For lymphatic function analysis using Qtracker™ 655 Vascular Labels uptake was measured inside the LFL at 3 h post-injection. Image analysis was carried out using ImageJ 2.0.0. ROIs were drawn on individual z-slices which included the main vessel of the LFL using the *Tg(prox1a:RFP)^{nm5}* channel. The mean pixel value calculated across the z-slices, which varied between 5–9 slices depending on the thickness of the vessel. This method differed from that of the FITC-dextran uptake experiment as Qtracker™ 655 Vascular Labels was more stable within the tissue and was not cleared at 3 h post-injection despite uptake into the tissue for some genotypic backgrounds.

Fluorescent intensity quantification

For fluorescent intensity quantifications, images used in Figure 2B were rendered in Imaris v9.3.0 with a surface detail of 0.75 μm using *Tg(-5.2lyve1b:DsRed2)^{nz101}*. Both channels were then masked and used for representative images. In the head, the distal section of the developing lymphatic sprout was isolated by hand using the Cut Surface tool. Strongly GFP-positive cells with a morphology distinct from endothelial (Figure S3G) were removed through rendering of *Tg(mafbbE1bas:EGFP)^{uu2kk}*. In the trunk, the PCV was rendered using *Tg(-5.2lyve1b:DsRed2)^{nz101}* and the sprouting vessels were trimmed manually. The average intensity of the trimmed rendered surfaces was calculated for both channels using the Statistics tool in Imaris v9.3.0. *Tg(-5.2lyve1b:DsRed2)^{nz101}* was confirmed not to change in intensity between the controls and MO-injected *Tg(-5.2lyve1b:DsRed2)^{nz101};Tg(mafbbE1bas:EGFP)^{uu2kk}* embryos (Figure S3H). The normalised GFP intensity value for each image was calculated by dividing the mean intensity value of the GFP channel by the mean intensity value of the DsRed channel in the rendered lymphatic surfaces. The normalized GFP values of every imaging session were then divided by the median of the controls of that session.

Average image analysis

Average image overlays were generated using MATLAB and elastix (Klein et al., 2010), with the method previously described (Allalou et al., 2017). Embryos of each genotypic group were aligned to generate an average pattern using Iterative Shape Averaging (ISA) algorithm (Rohlfing et al., 2001), and iteratively improved using an affine transformation and non-linear transformation.

Cell migration analysis

Movies were prepared for cell tracking in ImageJ using the Registration tool to account for drift during the course of imaging, then tracking was carried out using the Manual Tracking tool.

The Mean Squared Displacement (MSD) is computed by calculating the MSD for each frame as the sum of squared distances to the tip position for that frame, this is then divided by the number of objects.

Cell directionality was quantified by comparing the angle of each track to the first position of that track. This is then represented as an angle in the polar histogram. The angle interval for each sector (=bins) is set to 30 degrees, and the distance to the origin corresponds to the number of positions within that angle interval.

Statistical analysis

Normality of all numerical datasets was tested with a Shapiro-Wilk test. When the number of datapoints was lower than 5, the data were assumed not to be normally distributed.

For pair-wise comparison, an unpaired two-tailed Student's *t*-test was run on normally distributed data, while a Mann-Whitney test was run if normality was not confirmed. A Wilcoxon test was run on paired data.

For multiple comparisons, a one-way ANOVA was run on normally distributed data, while a Kruskal-Wallis test was run if normality was not confirmed. Both were run together with Dunn's multiple comparison test. When two independent variables were present, a two-way ANOVA with Sidak's multiple comparison test was used.

For qualitative data, a Chi-square test was used. For survival curves, a Gehan-Breslow-Wilcoxon test was used.